Atmos. Chem. Phys. Discuss., 3, 5875–5918, 2003
www.atmos-chem-phys.org/acpd/3/5875/

Atmospheric Chemistry and Physics Discussions

Analysis of a jet stream induced gravity wave associated with an observed ice cloud over Greenland

S. Buss[1], A. Hertzog[2], C. Hostettler[3], T. P. Bui[4], D. Lüthi[1], and H. Wernli[1]

[1]Institute for Atmospheric and Climate Science, Zürich, Switzerland
[2]Laboratoire de Météorologie Dynamique, Palaiseau, France
[3]NASA, Langley Research Center, Hampton VA, USA
[4]NASA Ames Research Center, Moffett Field CA, USA

Received: 23 September 2003 – Accepted: 13 November 2003 – Published: 18 November 2003

Correspondence to: S. Buss (sbuss@iac.umnw.ethz.ch)

Abstract

A polar stratospheric ice cloud (PSC type II) was observed by airborne lidar above Greenland on 14 January 2000. Is was the unique observation of an ice cloud over Greenland during the SOLVE/THESEO 2000 campaign. Mesoscale simulations with the hydrostatic HRM model are presented which, in contrast to global analyses, are capable to produce a vertically propagating gravity wave that induces the low temperatures at the level of the PSC afforded for the ice formation. The simulated minimum temperature is ∼8 K below the driving analyses and ∼3 K below the frost point, exactly coinciding with the location of the observed ice cloud. Despite the high elevations of the Greenland orography the simulated gravity wave is not a mountain wave. Analyses of the horizontal wind divergence, of the background wind profiles, of backward gravity wave ray-tracing trajectories, of HRM experiments with reduced Greenland topography and of several instability diagnostics near the tropopause level provide consistent evidence that the wave is emitted by the geostrophic adjustment of a jet instability associated with an intense, rapidly evolving, anticyclonically curved jet stream.

In order to evaluate the potential frequency of such non-orographic polar stratospheric cloud events, an approximate jet instability diagnostic is performed for the winter 1999/2000. It indicates that ice-PSCs are only occasionally generated by gravity waves emanating from an unstable jet.

1. Introduction

In situations where the large-scale stratospheric temperature is slightly above the thresholds for the existence of NAT (nitric acid trihydrate) or ice, inertio gravity waves can be effective in inducing PSCs. At the surface of PSC particles, heterogeneous chlorine activation might occur which in turn eventually destroys several hundreds stratospheric ozone molecules. Thus, in the last years, mountain gravity waves gained substantial consideration as model studies and observation confer them an important role

ACPD

3, 5875–5918, 2003

in stratospheric ozone depletion (Cariolle et al., 1989; Carslaw et al., 1998). Mountain wave-induced adiabatic expansion of air along tilted isentropes can lead to temperature differences of up to 13 K as compared to analyses which do not contain the wave signals (Dörnbrack et al., 1999) and may allow stratospheric temperature to drop below the ice formation threshold.

Recently, Hitchman et al. (2003) proposed an alternative Gravity Wave (GW) forcing mechanism important for PSC formation: waves emitted from breaking Rossby-waves with an associated unbalanced jet stream at the tropopause level can also lead to mesoscale temperatures fluctuations in the stratosphere sufficient to cool below the frost point (T_{ice}).

This article will report on an ice PSC recorded by the NASA DC-8 lidar during the transfer flight on 14 January 2000 from the NASA Dryden center to Kiruna (Northern Sweden), where the SOLVE/THESEO (SAGE III Ozone Loss and Validation Experiment/Third European Stratospheric Experiment on Ozone) campaign was hosted. It was the only ice-cloud observed over Greenland (GL) during the entire deployment. The temperatures from global analyses (i.e. from the European Center for Medium-Range Weather Forecast, ECMWF) are several degrees too high to explain the occurrence of ice at a height of about 23 km (see Fig. 1, top). A mesoscale GW which would not be resolved by global models could lead to the needed temperature decrease. This cloud observation (i) provides the fortuitous opportunity to investigate the capability of mesoscale models to realistically simulate the stratospheric temperature field over the complex and large-scale topography of GL and (ii) motivates the investigation of the dynamical mechanisms that were responsible for the generation of small scale patches with temperature T below T_{ice}. The main focus of the present study are the dynamics and modelling capabilities. The reader is referred to Luo et al. (2003) for through microphysical considerations of this ice cloud. Few hours after the DC-8 observation the NASA ER-2 aircraft also crossed GL during its transfer flight and observed an enhanced wind and temperature variance. This also could be attributed to a GW and delivers a further validation opportunity for the mesoscale model. In the remaining of

ACPD
3, 5875–5918, 2003

the introduction some general background on gravity wave generation mechanisms – a key aspect of the present study – is provided.

Gossard and Hooke (1975) review the following mechanisms that can act as energy sources for GWs: convection, density impulses (accelerating fronts), geostrophic adjustment, topographical forcing and vertical shear instability. For the present study, which deals with the high latitudes of GL during winter, convection can be ruled out as a GW forcing mechanism.

Several articles report observations of inertia GW which could be attributed to emanate from vertical shear instabilities, e.g. Thomas et al. (1999); Pavelin et al. (2001); Hertzog et al. (2001); Peters et al. (2003). In the cases discussed by Shibata et al. (2003) and Hitchman et al. (2003), the GWs induced near the level of an unbalanced jet stream let to the formation of PSCs as observed by lidars.

Uccellini and Koch (1987) analyzed 13 cases of wave events over the USA with horizontal wavelengths $\lambda_h > 30$ km which all were initiated by adjustment or instability. Analyzing eight cases of observed mesoscale variance enhancements in the temperature and horizontal wind velocity, Fritts and Nastrom (1991) found one case each due to topography and jet-stream instability. These two cases showed the largest mean variances in wind and temperature. On the other hand, the decomposition of hundreds of balloon soundings (Nastrom et al., 1997) indicated that the jet stream is not a significant source of GW for vertical wavenumber spectra in the power law range.

Using a hydrostatic spectral model O'Sullivan and Dunkerton (1995) were able to simulate the life cycle of inertia-GWs generated near the level of maximum wind speed, in the vicinity of the jet-stream exit region. In an other idealized setup, Sutherland and Peltier (1995) using nonlinear incompressible Boussinesq-flow simulations restricted to two dimensions, pointed out that a precondition for the onset of such an instability is that the maximum shear on the upper flank of the jet, which typically is situated near the tropopause is shifted downward by about 1 km into a region in which the static stability is small. By reviewing observations, theory and model studies, Knox (1996) showed the stark connection between strongly anticyclonic flow situation and

ACPD
3, 5875–5918, 2003

GW activity induced by geostrophic adjustment and inertial instability. With a two-dimensional incompressible Boussinesq model, Scinocca and Ford (2000) were able to simulate the Kelvin-Helmholz instabilities of the shear layer that engenders large-scale GW radiation.

In order to investigate the dynamical mechanisms that lead to the generation of observed GWs over GL on 14 January 2000, we have performed meteorological simulations, comprising the entire island. Mesoscale simulations of the southern tip of GL, for an event of mountain wave reaching the stratosphere in 1992, including validation with observations (which were presented and discussed by Chan et al., 1993) were already performed by Leutbecher et al. (2000).

In the following section, the limited-area model and its setup are presented. The lidar ice-cloud observations are shown in Sect. 3. Then, in Sect. 4, the second GW signature measured on the same day is introduced and the mesoscale simulations compared with observations. In Sect. 5 the mechanisms that produced both GWs are investigated and the wave signatures found in the mesoscale numerical experiment interpreted. Backward ray trajectories are displayed and discussed in Sect. 5.3. The more general potential for jet-induced GWs which might lead to PSC formation is estimated for one winter season in Sect. 6.

2. Meteorological models

In the following subsections the model data utilized in this study are described.

2.1. ECMWF analyses

The ECMWF operates a spectral meteorological model and uses a four-dimensional variational data assimilation scheme (4-D var) since November 1997 (Rabier et al., 2000). It makes use of the advanced microwave sounding unit data which greatly improved the Arctic stratospheric temperatures (ECMWF, 1999). The triangular trunca-

ACPD
3, 5875–5918, 2003

tion version T319 (corresponding to a grid size of ∼60 km) has been introduced in April 1998 and additional vertical levels in March 1999. Since then, the ECMWF model includes 60 levels, of which typically about 30 are in the stratosphere i.e. above the 2 pvu (potential vorticity units, $10^{-6}m^2s^{-1}K\,kg^{-1}$) tropopause for the considered latitudes and season.

These 6-hourly ECMWF analyses provided the initial conditions and lateral boundary data for the mesoscale simulations described below.

2.2. HRM

2.2.1. The model

The limited-area high resolution model (HRM) is the successor of the Europa-Modell (EM, Majewski, 1991). The EM was used operationally by the German and Swiss Weather Services until early 2001. In the hindcast mode, it is intensively applied for regional climate simulations (e.g. Lüthi et al., 1996). In this climate version, a 15-year integration over Europe revealed a good agreement of simulated precipitation with observations and other limited-area models (Frei et al., 2003). During the SOLVE/THESEO deployment, the HRM produced daily quasi-operational stratospheric forecasts to help mission planing. Fueglistaler et al. (2003) examined the mountain wave induced PSC event over Scandinavia on 25 January 2000 (see also Dörnbrack et al., 2002). Using a microphysical box model and trajectories from a HRM simulation, they could realistically reconstruct the observed lidar signals associated with the PSC.

The HRM integrates the set of primitive equations in the hydrostatic limit in hybrid pressure coordinates terrain-following sigma coordinates near the ground and constant p-levels in the stratosphere. The prognostic variables are perturbation pressure, temperature, the three wind components as well as specific humidity and cloud liquid water content. The full physics form includes parametrizations of radiation and convection (Majewski, 1991).

A linear fourth order diffusion is applied in the horizontal to ensure numerical stability.

ACPD
3, 5875–5918, 2003

The diffusion is scale selective, where only the waves up to four times the mesh width are noticeably attenuated. As the fourth order diffusion corresponds to a five points-operator, a second order diffusion is applied at the borders of the domain. In the vertical direction, the diffusion parametrization is based on a flux-gradient approach in which the turbulent vertical fluxes are proportional to the vertical gradient of the variable to be attenuated and a diffusion coefficient. The computation of the turbulent vertical diffusion coefficients is based upon the second order closure of the equations for higher moments.

The HRM has been tested for flow past obstacles in idealized conditions (Lüthi, 1994). The response of a uniform, constantly stratified, adiabatic and inviscid flow to a bell-shaped, isolated mountain was found to be in good agreement with analytical solutions. The radiative upper boundary condition of the model based on Bougeault (1983) and Klemp and Durran (1983) (see Herzog (1995) for its application to hybrid coordinates) was found suitable and showed no sign of spurious reflection.

2.2.2. Setup of the GL simulations

Firstly, the discussion is restricted on a dry physics simulation without convection initialized on 13 January 2000, 12:00 UTC which includes the other parametrizations (soil processes, radiation and turbulence). The simulation is performed for 30 h with a computational time step of 25 s and output is produced every hour. Sensitivity experiments, for a wide range of parameters (which will be discussed in the Appendix), showed for instance that inclusion of moist thermodynamics and the exclusion of radiation have in the present case, little or no effect on modeling the generation of GWs and their propagation into the stratosphere.

The model orography is derived from the 30″ spaced elevation data set from the U.S. Geological Survey, Sioux Falls, South Dakota. For the present simulation, a Gaussian filter is applied to the orography in order to reduce the short wavelength contributions to the mountain waves, as finite differencing errors are large for waves with wavelength close to twice the mesh width.

In the stratosphere a relatively high vertical resolution is necessary in order to resolve GWs, as their vertical wavelength might become small due to high static stability. Therefore an equidistant level spacing of approximately $\Delta z \approx 700$ m has been chosen throughout the model atmosphere. There are 60 vertical levels in total with the model top at 2 hPa (∼42 km). The horizontal resolution is $\Delta x = 0.125^\circ$ which corresponds to ∼14 km and the simulation comprises the entire island of GL (145×201 grid points, see Fig. 4 for a view of the domain). Simulations for such large a domain (∼800×3000 km) are challenging and the lidar and ER-2 in-situ observations provide the possibility to validate aspects of the numerical experiments.

3. Ice cloud above GL on 14 January 2000

3.1. Lidar observation

During the forementioned flight, the NASA DC-8 LaRC Aerosol lidar (a piggy-back instrument measuring backscatter ratios (BSR) at 354 nm and 1064 nm as well as depolarization at 532 nm) recorded both types of PSCs above GL. The lidar recordings of the flight segment within the mesoscale simulation domain (see Fig. 4) are shown in Fig. 1. For a backscatter ratio (BSR) at 1064 nm greater then 50 (red), water ice (PSC type II) can safely be assumed due to the large amount of condensated mass, and low values (BSR lower than 30, green and dark blue) indicate the presence of supercooled ternary solution (STS) droplets (PSC type I). The ice cloud near 23° W, 77° N at an altitude of ∼23 km (corresponding to ∼25 hPa or ∼520 K) has a horizontal extension in the aircraft flight direction of ∼50 km and is the central feature of the present investigation. It's horizontal location is in the center of the white box indicated in Fig. 4 and is close to the eastern coast of Greenland.

The ECMWF temperatures (overlayed contours in the upper panel of Fig. 1) are too high to allow ice formation: at the height of the observed ice cloud the ECMWF temperature is ∼189 K which is more than 3 K above the frost point at 25 hPa (assuming

ACPD
3, 5875–5918, 2003

a water mixing ratio of 6 ppmv). For the homogeneous formation of ice particles, temperatures even ∼3 K below the frost point (i.e. ∼ 183 K) would be required (Koop et al., 2000).

The disposal of the single PSC lidar signals suggests that gravity waves could account for the regular appearance of the required cold patches, namely with a vertical and horizontal wavelengths of the order $\lambda_z \sim 4$ and $\lambda_h \sim 180$ km. Closer inspection of the ice cloud reveals that a wave train with much smaller scale, $\lambda_h \sim 15$ km, is superimposed. We hypothesize that this fine-scale features are associated with vertically propagating GWs triggered by the complex structure of the underlying topography. However, these structures have too small a scale to be resolved by a hydrostatic model for the entire GL island. Therefore, the model analyses will be restricted to the interpretation of the ice cloud as a whole and not on its internal structure.

3.2. Air trajectory

The cooling rate of air parcels involved in the PSC formation is an important factor determining the cloud's microphysical composition. Here we use the HRM simulation output which (in contrast to ECMWF) provides a realistic stratospheric temperature field for this particular case (as discussed in Sect. 4.2).

In order to estimate the cooling rate that air parcels undergo as they become part of the ice cloud, we computed an air trajectory from the location (22.6° W, 77.3° N) and time (08:00 UTC) of maximum observed BSR (c.f. Fig. 1), backward and forward in time, with the HRM wind fields. A description of the trajectory calculation tool can be found in Wernli and Davies (1997). The temperature as well as the cooling/warming rate along the trajectory are shown in Fig. 2 and the horizontal trace of the trajectory is drawn in Fig. 4 (top, black line). The air parcels' temperature oscillations have a time scale of about 2 hours whilst traveling over GL, possibly due to GWs, and only for a short time period (<1 h) temperature goes below T_{ice}. 1 h after the occurrence of the PSC the air has warmed by 13 K and T exceeds also the threshold for the existence of NAT. Note also in Fig. 2a the striking difference of the temperature experimenced by

the PSC air parcel and the more slowly varying local temperature evolution.

The cooling rate (Fig. 2b) at the onset of nucleation controls the resulting ice particle number density. Here, the high high rates ($> 40\,\mathrm{K h^{-1}}$) lead to freezing of the great majority of the liquid ternary solution droplets, resulting in an ice PSC with particle number density $n{\sim}10^1\mathrm{cm}^{-3}$ (Fueglistaler et al., 2003). This cooling rate stays in good agreement with those found by Luo et al. (2003), who derived a trajectory quantitatively from the lidar PSC measurement.

The calculated cooling rates exceed the ones quoted by Shibata et al. (2003) and would not lead to substantial dehydration due to the small particle sizes and the short lifetime of the ice particles of ∼0.5 h. The sedimenting velocity of particles with radii $\sim 1\,\mu$m is about $1\,\mathrm{m h^{-1}}$, thus the fall distance is less than 1 m. It has been suggested that NAT can nucleate on ice particles (Carslaw et al., 1998; Luo et al., 2003). Based on the temperature history along the trajectory (Fig. 2a), the air parcel remains below the equilibrium temperature for NAT (Hanson and Mauersberger, 1988) only about one hour and thereafter particles will evaporate rapidly. This duration is too short for substantial denitrification induced by this particular ice cloud. A detailed discussion of the microphysical life cycle of other PSCs' particles can be found in Fueglistaler et al. (2003) and Luo et al. (2003).

3.3. The synoptic situation

Here, using ECMWF analyses data, we present the synoptic situation in the region of GL during the monthes prior to the ice cloud observation. From 13 January, 18:00 UTC (Fig. 3a) through 14 January, 06:00 UTC (Fig. 3b) and further to 15 January, a pronounced upper tropospheric ridge shifts northeastwards from the southeast of GL, as seen by the protruding tongue of low PV air on the 320 K isentrope. This ridge initiated already on 12 January 2000 and transformed into a mid-tropospheric anticyclone on 16 January with closed 500 hPa-geopotential isolines (not shown). This anticyclone is associated with a negative upper-level PV-anomaly (Schwierz, 2001) and remains quasi-stationary between GL and Europe until the 25th of January.

The jet-stream which goes along with the region of maximum PV gradients is very intense and strongly curved. On the 370 hPa surface, wind speeds exceed 60 m s^{-1} in the vicinity of the tropopause (see the blue contours). At 18:00 UTC on 13 January (Fig. 3a), there is strong deflection between the S–N aligned jet streak south of GL and the westerly jet streak across GL further north. 12 h later (Fig. 3b), upper level winds blow about parallel to the SE coast of GL and a northerly jet streak has formed NE of Iceland. Generally, the synoptic situation in the GL region has a strong non-stationary character during this time period.

As underlined by Knox (1996), strong anticyclonically curved flows may be regions with large vertical shears. These regions, by means of geostrophic adjustment and inertial instability offer mechanisms for GW generation. This is also in line with results from Kaplan and Paine (1977) who noted decreasing dynamic stability in a case where a jet streak approached an upper-level ridge.

In the lower troposphere, a slowly evolving low-pressure system develops from the 13th to the 15th January on the south-western tip of GL producing a southerly surface flow south of the island (see wind vectors in Fig. 3). These intense low-level winds across GL (up to 20 m s^{-1}) in principle favor the orographic generation of vertically propagating GWs.

At around 26 km height the vortex edge is approximatively zonally aligned (see purple contours in Fig. 3). Parallel alignment of the tropospheric and stratospheric jets privileges the vertical propagation of GWs (irrespective of the generation mechanism) and can lead to enhanced GW-induced temperature perturbations in the stratosphere (Whiteway and Duck, 1999).

4. Wave signatures in the HRM simulations

In this section GW structures in the HRM simulation are explored. The focus is (i) on the GW that led to the formation of the ice PSC observed by the lidar on board the DC-8 (this GW will be referred to as “wave DC8” hereinafter), and (ii) to GWs identified

ACPD
3, 5875–5918, 2003

from the ER-2 in-situ measurements (in the following "wave ER2"). The observations serve also to quantitatively validate aspects of the model simulation.

4.1. Horizontal views of mesoscale temperatures

A horizontal view of the HRM temperature field at the time (07:00 UTC, 14 January, 17 h after the start of the simulation) and height (23 km) of the maximum observed lidar BSR (Fig. 1) indicates rich mesoscale patterns. Several spots exist over GL with stratospheric temperatures low enough to allow PSC type II formation (T<183 K; Fig. 4, top). Vertical sections through these potential locations of ice-clouds (not shown) exhibit evidence that they do stem neither from a single horizontally propagating wave nor from a unique source with different propagation angles, but that each has its own origin. Note that the southernmost cold location (~32° W, ~72° N) has been sampled by the ER-2 about eleven hours later, when the wave activity has weakened in the mesoscale model. Figure 4 (bottom) shows the HRM temperatures at the time (18:00 UTC) and flight altitude (19.3 km) of the ER2 observation. Here also, the HRM produces vertically propagating GWs at the location of temperature and wind variance enhancement observed by the ER-2 (see also Fig. 5).

4.2. Model validation with observations

The vertical section of HRM temperature along the DC-8 flight path (Fig. 1, bottom) reveals clear GW signals leading to large deviations from the ECMWF analyses (compare with Fig. 1, top). Near 23° W, the mesoscale simulation produces a temperature minimum 8 K colder than the analyses (and ~4.5 K below the frost point), at the exact location of the ice cloud. This is in good agreement with Luo et al. (2003) who estimated mesoscale temperature variations of ±7 K with respect to the ECMWF analyses, by matching BSR of ice particles obtained from a microphysical model to the measured BSR aboard the DC-8. The horizontal and vertical extension of the ice cloud, as seen in the lidar plane, is also very well reproduced by the HRM. The other (type I) clouds

ACPD
3, 5875–5918, 2003

observed by the lidar do not always exactly correspond to, but are close to a local HRM temperature minimum.

Aboard the ER-2, the meteorological measurement system (MMS) is collecting data with a sampling rate of 10 Hz and an uncertainty of 0.3 K for temperature and 1 ms^{-1} for the airspeed (Scott et al., 1990). This yields low-pass filtered data at a resolution of 1 s or ∼200 m horizontal distance at mean cruise speed. The MMS temperature, zonal and meridional wind observations are displayed in Fig. 5 along with the HRM simulation and ECMWF analyses interpolated in time and space to the flight path. The limitations of the HRM resolution (15 km in space and 1 h in time) indicate that no perfect agreement with the observations can be expected on the smallest scales. The observations show enhanced temperature and wind variance around 30° W which can be identified as a GW signature, as noted by Chan et al. (1993). HRM temperatures and winds also show enhanced fluctuations at the right location, however with too long a horizontal wavelength. They oscillate around the driving ECMWF analyses, and thus, if the analyses are biased (positively at the beginning and end of the considered flight segment) the (fluctuating) mesoscale temperatures and winds are likely to show the same bias. The overall HRM differences with respect to the observations are weakly positive for temperatures (less than 1 K with a standard deviation of 1.7 K) and slightly negative for wind velocity of ($-0.7\ ms^{-1}$).

These qualitative and quantitative comparisons of HRM temperatures and winds with the available independant measurements, point to the capability of the HRM to produce accurate propagating GWs above GL up to the middle stratosphere and completes the validation of this HRM simulation.

5. Interpretation of HRM wave signatures

Various diagnostic techniques are applied to the HRM model output in order to obtain evidence for the origin of the two GW structures (“wave DC8”, “wave ER2”) discussed in the last sections. The diagnostics mainly include analysis of wind profiles, investigation

ACPD
3, 5875–5918, 2003

of the waves' divergence patterns and detailed GW ray tracing calculations.

5.1. Wind profiles

We first look at the background wind profiles from ECMWF analyses averaged within the boxes shown in Fig. 4, just around the observations of "wave DC8" and "wave ER2". Panels a and c of Fig. 6 show the velocity profiles few hours prior to the time of observation (solid line) as compared to the monthly mean (dashed lines) within the boxes. Note the very strong jets near 250 and 7 hPa around the ER-2 observation. Panels b and d show the mean wind directions within the boxes. In Fig. 6b the change of wind direction with height of more than 90° in the layer from 800 to 500 hPa points to the existence of a critical layer which prevents mountain waves to propagate upward into the stratosphere. In contrast, within the box around "wave ER2" (panel d), the wind direction changes less with height and the wind profile allows vertical wave propagation from the surface to the middle stratosphere. These wind profiles are a first indication that "wave ER2" can be a quasi-vertically propagating mountain wave whereas "wave DC8" cannot.

Within the same boxes and using now the HRM wind fields, the vertical eddy momentum fluxes were estimated (not shown). The momentum flux of "wave ER2" is almost constant both in height and time, from 00:00 to 18:00 UTC, 14 January 2000. In contrast, the flux of "wave DC8" changes twice its sign from the bottom to the top level, during the entire period between 18:00 UTC, 13 January and 12:00 UTC, 14 January. The first level of zero flux is near 500 hPa and consistent with the mid-tropospheric critical level identified in Fig. 6b. Near the tropopause, around 300 hPa the vertical momentum flux again changes its sign. The intrinsic frequency of a wave packet that approaches a critical level goes to zero. Thus the wave packet is neither transmitted nor reflected (Bretherton, 1969) and the momentum transported by a wave vanishes near this level. This brief analysis of vertical momentum flux profiles also points to an orographic source for "wave ER2" and gives an indication of the possible origin of "wave DC8", around the 300 hPa level.

ACPD
3, 5875–5918, 2003

5.2. Divergence along flight tracks

The horizontal wind divergence calculated from the HRM simulations is shown in Fig. 7 along the two flight paths for 14 January, 07:00 UTC (top, "wave DC8") and 18:00 UTC (bottom, "wave ER2"). The alternation of convergence and divergence as well as the back tilt of the constant phase lines are characteristic of vertically propagating GWs. For "wave ER2", vertical coherency is obvious from the GL mountains to the model top and thus, this wave is due to an orographic forcing. For "wave DC8", the patterns confirm the findings from previous section: this wave is not a mountain wave and its origin is situated around 300 hPa. Note that from Fig. 7, "wave DC8" appears to be horizontally more extended and has a larger horizontal and a smaller vertical wavelength than "wave ER2".

Figure 8 shows the same vertical sections as Fig. 7, but for a HRM experiment for which the height of the GL topography has been reduced by 25%, leading to a maximum GL elevation of 2367 instead of 3155 m. It shows that while "wave DC8" is scarcely affected, the divergence signature of "wave ER2" almost disappears in this sensitivity experiment. This confirms the above hypothesis about the origin of both waves.

In order to further corroborate the jet-stream origin of "wave DC8", backward ray trajectories will be computed in the section.

5.3. GW ray tracing

Here we apply the GW ray tracing technique (Hertzog et al., 2001) to our "wave DC8" case. This technique has proven to be useful for determining the source of stratospheric GW signals (Hertzog et al., 2001). To compute an ensemble of backward ray trajectories, the initial wave specifications (direction of propagation, intrinsic frequency and vertical wavelength or the three wavenumbers) are requested. The way these are derived is exposed in the following section and then the results of the ray tracing are presented.

ACPD
3, 5875–5918, 2003

5.3.1. Wave specifications

The following procedure has been applied to determine the characteristics of the (supposed monochromatic) wave packet at the time and location of the ice cloud observation. At this time and location, a vertical sounding has been performed through the HRM model atmosphere. The resulting zonal and meridional wind profiles are shown in Fig. 9a. The horizontal velocity vector rotates anticyclonically with height, which is consistent with an upward energy propagation and a negative vertical wavenumber m (using the convention that the intrinsic frequency ω_0 is positive).

In order to derive the wind oscillations induced by the gravity wave, a linear fit (thin line in Fig. 9a within the range 13 to 34 km) has been subtracted from the actual profiles to obtain the wind and temperature perturbations which are displayed in Fig. 9b. For the present case, this method provided a more consistent and robust signal then the hodograph method used for instance by O'Sullivan and Dunkerton (1995) and Hertzog et al. (2001). Reasonable estimation for the vertical wavelength can be obtained from the different variables and height ranges (Fig. 9a or b) leading to λ_z=8000±1200 m.

Then, to determine the correct wave propagation angle, we varied it between 0 and 179° (0° stays for eastwards wave propagation) and identified the angle with the maximum variance of the wind parallel to it (see Fig. 9c). The wind components have therefore been projected to the parallel and perpendicular direction of the propagation angle, between 21 and 28 km, which is the height range where the wave signal can clearest be identified in the considered fields (see also Fig. 1). It turns out that an unambiguous maximum exists for Θ=7° for which the parallel wind variance (solid line) reaches 72 $m^2 s^{-2}$. Now, the polarization equation (Andrews et al., 1987),

$$\begin{bmatrix} u\prime \\ v\prime \end{bmatrix} = A[R(\Theta)] \begin{bmatrix} cos(mz+\phi) \\ -\frac{f}{\omega_0} sin(mz+\phi) \end{bmatrix}, \quad (1)$$

state that the ratio between the propagation parallel and perpendicular wind variances are equal to ω_0/f, where f is the Coriolis parameter. $[R(\Theta)]$ is the rotation matrix

ACPD
3, 5875–5918, 2003

which allows the phase speed to be aligned with the propagation direction, A is the wave amplitude and ϕ a phase-shift. In our case, the ratio for $\Theta=7^\circ$ is $\omega_0/f=3.3$, which yields an intrinsic period of $2\pi/\omega_0=3.72$ h. In agreement with the assumption of an inertio GW in the rotating wave regime (as $f \lesssim \omega_0 \ll N$, with N the Brunt Väisäla frequency).

The hydrostatic dispersion relation reads

$$m^2 = \frac{N^2 - \omega_0^2}{\omega_0^2 - f^2}(k^2 + l^2), \quad (2)$$

where k and l are the zonal and meridional wave numbers, and knowing that $\|\tan\Theta\|=\|l/k\|$, wavelengths can be estimated, leading to $2\pi/k = \lambda_x$=387 km and $2\pi/l = \lambda_y$=3149 km.

There remains an ambiguity of $\pm 180^\circ$ about the propagation direction, or in other words in the sign of the horizontal wave numbers. This can be removed with the help of the Doppler shift between the wave intrinsic and apparent frequencies (ω), both of which are linked through: $\omega = \omega_0 + ku + lv$. At the cloud location and time of observation, the ECMWF analyses give $u\sim 45$ and $v\sim -7\,\mathrm{ms}^{-1}$. Therefore, the apparent period of the wave packet is $\|2\pi/\omega\|\sim 10$ h. Independently, the wave apparent period can be estimated from the time evolution of the temperature at a fixed location (Fig. 2a). For $k<0$ ($k>0$), the calculated apparent period is $-16.3 \leq 2\pi/\omega \leq -4.5$ h ($1.3\leq 2\pi/\omega \leq 1.7$ h). Clearly, positive wavenumbers cannot explain the existing Doppler shift and therefore $k<0$. Furthermore, as the wave vector is aligned with the direction of propagation, $k<0$ also implies that $l<0$, thus the effective propagation angle is $\Theta= -173^\circ$ and the horizontal wave vector is directed towards west-south-west. For simplicity, the ray trajectory computed from this first estimation of the wave parameters, k, l and m (see Table 1) will be referred to as "first guess ray" hereinafter. Observe that the apparent frequency determined from the temperature evolution at the location of cloud observation and estimated from the Doppler shift equation differ, but have the same order of magnitude. We will account for this discrepancy by starting an ensemble

ACPD
3, 5875–5918, 2003

of rays, as described below.

In ray-tracing calculations, the major source of error comes from the initial conditions, i.e. the wave specifications settled by the three wave numbers. In order to take account of such errors, we started an ensemble of ray trajectories, with initial conditions given by the uncertainties of the wave parameters, which we estimated generously. The wave parameters along with their estimated uncertainties are summarized in Table 1. We allowed λ_z to vary between 6.8 and 9.2 km, in steps of 400 m and Θ and ω_0/f as indicated in Table 1, with each 5 possible values. In total, this yields 175 initial conditions. As a consequence, the zonal (meridional) wavelength varies between 245 and 685 (1280 and 12 875) km. The only parameters we assumed to be perfectly known are the time, height, longitude and latitude of observation. Because the ray trajectories were found to be little sensitive to their initial height within the range z_0=23 ± 1 km, all trajectories were initiated at 23 km, 22.6 W and 77.3 N at 14 Janury, 07:30 UTC. Background fields (horizontal winds and static stability) necessary for the integration are taken from the ECMWF analyses.

5.3.2. Results

The results are depicted in Fig. 10 for all 175 backward wave trajectories, with the "first guess ray" indicated in red, and the horizontal projection of the ray trajectories are shown in Fig. 12b. From the 175 ensemble members, there are 57 trajectories which remain in the stratosphere at least until 13 January, 00:00 UTC and never reach a height below 9 km. They will not be considered in the following discussion. From all trajectories reaching the troposphere none comes from ground levels above mountainous terrain. Thus, according to these ray trajectories, an orographic origin of "wave DC8" can be ruled out.

In the very first hours of integration, as the wave packet descends and its vertical wavelength decreases, every ray encountered a caustic, indicated by a change of sign in the action density (not shown). Nevertheless, Broutman (1986) shows that the ray-tracing equations can still produce valid results after the caustic, as suggested by the

ACPD
3, 5875–5918, 2003

smooth horizontal trace of the rays.

Note that the vertical wavelength of the "first guess ray" (as of the other rays) rapidly decreases and drops to 5 km after 2.5 h of back-propagation (corresponding altitude of 20 km). This is in nice quantitative agreement with the two levels of PSC in the lidar observations at about 18.5 and 23 km (see Fig. 1). This change in vertical wavelength might provide an explanation of why no cloud is observed above 23 km: actually, if λ_z remained constant (5 km), clouds would be expected at ~27 km height as the synoptic temperatures are very close to those at ~19 km (Fig. 1), the first floor of PSCs.

After 6–12 h backward in time most of the ensemble's trajectories pass through the tropopause jet (which coincides with the increase in the vertical wavelength and intrinsic frequency to increase). For the "first guess ray", the wind speed at this moment exceeds 60 ms^{-1} (Fig. 10c) with a strong northerly component (Fig. 10b). (The mean and standard deviation of the wind velocity for the ensemble is 55±5 ms^{-1}) As this ray continues to descend, it reaches the positive shear layer where the Richardson number, Ri, becomes <1 in the ECMWF as well as in the HRM (Fig. 10f). (For the ray ensemble the averaged minimum HRM Richardson number becomes 2.1±1.7.) Ri is a dynamically significant stability and turbulence indicator. Instability can be expected where Ri is smaller than a certain threshold value. Calculated from gridded data fields, this threshold depends on resolution, and is taken typically as Ri_c=2 in mesoscale models with resolutions of ~10 km.

For the "first guess ray", we identified its most probable location of wave generation where Ri attains its minimum along the ray. This occurs at $t = -13\,h$, near the 370 hPa pressure level, or 300 K isentrope (see crosses in Figs. 10 and 11). This location coincides with the region of maximum vertical shear and low static stability (see Fig. 11), which is also a prerequisite for the onset of strong turbulence. Despite the dispersion of the ray trajectories, 85% of the ensemble members reaching the troposphere do attain their minimum in Ri in a very similar situation as the "first guess ray" (shown in Fig. 11), i.e. low static stability and large positive vertical shear, beneath the jet core. In this sense the "first guess ray" is representative of the actual trajectory of the wave

ACPD
3, 5875–5918, 2003

packet.

Note further in Fig. 11 that the "first guess ray" passes very close to a tropopause fold. Using a two-dimensional, isentropic primitive equation model, Gidel and Shapiro (1979) showed that two patches of turbulence are associated with tropopause folds: one in the stratosphere above the jet core and one, stronger, situated in the troposphere below the jet axis. The fact that the ray hits an intense jet-stream, associated with a tropopause fold is a further piece of evidence that "wave DC8" is emitted from a vertical shear layer.

The horizontal trace of the "first guess ray" (shown only until the minimum Richardson number, Fig. 12a) indicates that the wave has been generated on the northern side of the jet, characterized by cyclonic horizontal shear. Further, the horizontal trace ends close to the left exit region of the previously noted tropospheric southerly jet streak (compare with Fig. 3a) which is also a preferred region for wave emission (O'Sullivan and Dunkerton, 1995; Thomas et al., 1999).

5.4. Instability diagnostics

A final step of our analysis of the dynamical origin of "wave DC8" is a brief analysis of the dynamical stability characteristics of the tropopause-level jet-streak. To this end, three diagnostics are calculated as suggested by previous studies of jet-stream instabilites (Zhang et al., 2000; Hertzog et al., 2001): the Lagrangian Rossby number, Richardson number and the residual of the non-linear balance equation. As the theoretical understanding of vertical shear instability is still limited, these quantitites should be regarded as useful proxies instead of rigid criteria for GW generation.

First, Fig. 12a shows a horizontal view of Ri at the time and level of the supposed wave generation. In agreement with the discussion in the previous section, the westerly jet streak is associated with very low values (Ri<1) and it is within or close to this narrow band that most of the ray trajectories cross the tropopause level.

Second, the Lagrangian Rossby number, Ro, was computed according to e.g.

ACPD
3, 5875–5918, 2003

O'Sullivan and Dunkerton (1995)

$$Ro = \frac{\|\frac{\partial \mathbf{V}}{\partial t}\|}{f\|\mathbf{V}\|} \tag{3}$$

with **V** being the horizontal wind vector. O'Sullivan and Dunkerton (1995) found that GW generation occurred in regions where $Ro \gtrsim 0.2$. This condition is not perfectly fulfilled for our ray trajectories (see Fig. 12c), although they pass closely to a region with large Ro.

Finally the non-linear balance equation (NBE), derived from the full divergence tendency equation in the case that its advection, the non-linear effects of divergence and the contributions of vertical motion gradients can be neglected, is also a measure of the flow's imbalance, and is given by

$$2J(u,v) - \beta u + f\zeta - \nabla^2\Phi = 0 \tag{4}$$

where J stays for the Jacobian, ζ is the relative vorticity and $\nabla^2\Phi$ stands for the horizontal Laplacian of the geopotential. Deviations from this balance condition, i.e. the residuum of Eq. (4), is also a measure for the flow's potential instability. Figure 12b shows the residual of Eq. (4) on the 370 hPa surface computed with ECMWF analysis along with the full length of the ensemble rays. The region of maximum imbalance predicted by the NBE is located somewhat eastward of the region where the wave packets were presumably generated and slightly to the north of the maximum Ro. However, the patch with largest deviations from non-linear balance corresponds quite nicely with the band of small Ri and the ensemble rays all travel through a region with substantial (although not maximum) diagnosed jet-stream unbalance. Taken together, these brief diagnostics are supportive of our claim that "wave DC8" is generated by the geostrophic adjustment of an unbalanced intense jet.

ACPD
3, 5875–5918, 2003

6. Potential for jet-induced GW in winter climatology

In order to estimate the likely frequency and potential importance of ice clouds generated by shear instabilities, we have applied the NBE (Eq. 4) diagnostics to the entire winter from the beginning of December 1999 to the end of March 2000. We have chosen a residual threshold of $4{\cdot}10^{-4}\,s^{-2}$ and applied this threshold within the 100 to 500 hPa vertical layer in the northern hemisphere (20–90° N) to the 6 h ECMWF analyses.

The probability that for a given day and longitude (latitude), at least one time step and one model level within the height range exceeds the chosen threshold is shown in the upper (lower) panel of Fig. 13. In is shown that, mainly in January 2000, instability are diagnosed at high latitudes. Note that the discussed case on 14 January is associated with a strong signal in this proxy climatology, as compared to other events at high latitudes during this winter. The climatology indicates that jet induced GWs may be frequent, but mainly in the southernmost part of the Eurasian continent and the subtropical Pacific jet. In regions with the possibility for GWs to generate PSCs, say north of 60° N, unstable jet events are relatively rare (~3 events during the considered period).

Generally the time evolution of the potential instability regions indicates eastward propagation with the same order of magnitude than the synoptic weather systems (Fig. 13, top). In the meridional direction, (Fig. 13, bottom) it appears that several instability regions describe an anticyclonic propagation, in agreement with the results of Knox (1996).

Better understanding of the physical processes that lead to the occurence of vertical shear instabilities would be strongly desirable and could lead to a better substantiated criterion for the identification of jet-induced GWs.

ACPD
3, 5875–5918, 2003

7. Conclusions

Using meteorological data from ECMWF analyses and mesoscale HRM hindcast simulations, we investigated the dynamical mechanisms that generated two vertically propagating gravity waves. "Wave ER2" was undoubtfully generated by the orography and we have given consistent evidence that "wave DC8" was instigated by the geostrophic adjustment of a jet instability. In particular, we detected that the tropopause-level and surface synoptic features were very similar to the 13 jet-induced GW cases reviewed in Uccellini and Koch (1987): a surface low upstream of the wave activity with an associated northeast-southwest oriented distinct frontal boundary and wave generation at the exit region of an intense jet streak. Furthermore, the most plausible location of wave production was in the very vicinity of a tropopause fold associated with the strong jet. Little or no doubts remain on the contribution of this non-orographic inertio gravity wave to the low temperatures allowing the formation of the ice cloud.

The issue that remains is whether this wave has sufficient amplitude to explain the ~8 K mesoscale cooling or if a superimposed (orographic) wave also contributed to the temperature minimum responsible for the PSC formation. The lidar signal gives certainty that mountain waves with a horizontal scale of ~15 km (not resolved by the hydrostatic HRM) propagate until the cloud location.

The mesoscale model HRM was found to be a suited model for the simulation of vertically propagating waves which, in the present study, applies for two different wave generation mechanisms. In particular, the model simulation captured very well the amplitude and location of the cold spot with $T < T_{ice}$. Sensitivity experiments (see Appendix) revealed that the model results are particularly sensitive to the horizontal diffusion and initialization time.

In line with the recent studies of Hitchman et al. (2003) and Shibata et al. (2003) this study indicates that mesoscale PSCs can be induced not only by orographically triggered GWs but also via an alternative mechanism that is related to the rapid evolution of intense and curved jet streams near the tropopause level. It remains for further work

ACPD
3, 5875–5918, 2003

to quantify the relevance of the two mechanisms. Our preliminary attempt to count the potential jet-instability events in the polar regions during one winter indicates that they occur only sporadically.

Appendix: Sensitive dependencies to model parameters

Eleven numerical sensitivity experiments have been conducted to test the dependencies of the HRM simulations to several model parameters and processes. Compared to the original simulation discussed in the paper (in the following called control run), they were undertaken changing one parameter each time. These comprise changes of the horizontal and vertical resolution, variations in horizontal diffusion, modifications in the initialization time and inclusion or not of physical parametrizations. Table 2 summarizes the eleven experiments along with the minimum modeled temperatures at the locations of the observed waves. These experiments are discussed hereafter.

Initialization. The choice of the initialization time of a simulation is subtle when comparing with observations at a particular time. The longer the run, the more the mesoscale model will develop its own dynamics and might drift away from the driving analyses. On the other hand, too late a starting time of the simulation may prevent the mesoscale features (as GWs) to develop and fully propagate. Four runs with initialization prior to the initialization of the control run two runs with initialization after the 13 January 2000, 12L00 UTC have been performed to evaluate this significant sensitivity (see Table 2).

For the temperature at the location of the cloud observed by the DC-8, the minimum is achieved with the control simulation. The more the simulation is initialized earlier or later, the more the amplitude of the wave decreases and the higher becomes the minimum mesoscale temperature. Note also the slight vertical shift in the height of minimum temperature at this location as the initialization moves away from the control run. For the experiment started on 14 January, 00:00 UTC, the DC8 wave structure becomes hardly identifiable (e.g. in vertical sections similar to the ones shown in Figs. 1

ACPD
3, 5875–5918, 2003

and 7) which expresses either that the onset of the wave was missed or that the GW had no time to propagate to the flight path. From the ray-tracing simulations the former is more likely the case.

A similar behavior, even if less marked is found for the minimum temperature associated with "wave ER2". The simulation which produces the minimum temperature was initialized six hours before the control run.

Resolution. In order to test the impact of vertical resolution, the number of vertical levels was reduced a factor of two, the model top kept unchanged. "Wave DC8" appears to be emitted properly but dissipates prior to reach the cloud altitude. There, an upward shifted temperature minimum exists but the wave structure cannot be recognized any longer. This is in good agreement with the ray tracing model (see Fig. 10b) which indicated that at the moment of emission the vertical wavelength was smaller than at the moment of observation. The effect of the vertical resolution on the "wave ER2" with larger vertical wavelength is negligible.

Repeating the control run with doubled horizontal mesh width, roughly extinguishes "wave ER2" as revealed by an equivalent to Fig. 7. However this simulation delivers the absolute minimum temperature associated with "wave DC8" of all simulations.

Diffusion. In this experiment, the horizontal diffusion coefficients were increased by an order of magnitude. The effect on "wave DC8" is dramatic as its temperature minimum increases by 4 K while the effect on the minimum temperature associated with "wave ER2" was astonishingly a cooling of 1.5 K. A plausible explanation is that the wave encounters less destructive interference with other short wavelengths waves, since these are filtered by the strong diffusion as seen in an equivalent of Fig. 7. O'Sullivan and Dunkerton (1995) established that inertio GW are primarily sensitive to horizontal hyperdiffusion. Here, not only the amplitude of "wave DC8" was reduced but also its vertical wavelength

Physical parametrizations. The inclusion of convection or the exclusion of the radiation scheme in the simulation gave strikingly similar wave characteristics. These processes have no influence on the generation and propagation of GW up to the strato-

ACPD
3, 5875–5918, 2003

sphere at least for the present setup. This is not the case for the inclusion of moisture: the diabatic effects associated with the evaporation and condensation of water impinged on the simulated temperatures.

Acknowledgements. SB was partially supported through the EC-project THESEO-2000/EuroSOLVE (under contract BBW 99.0218-2, EVK2-CT-1999-00047) and through an ETHZ-internal research project.

We thank the ECMWF, MeteoSwiss, and the GSFC DAAC for providing access to the meteorological data. We are also very grateful to the ETHZ Cray staff for accommodating the large computational resources needed for the HRM simulations. Particularly acknowledged are S. Fueglistaler and T. Peter for the fruitful discussions.

References

Andrews, D. G., Holton, J. R., and Leovy, C. B.: Middle atmosphere dynamics, Academic Press, San Diego, 489, 1987. 5890

Bougeault, P.: A non-reflective upper boundary condition for limited area grid, Mon. Wea. Rev., 111, 420–429, 1983. 5881

Bretherton, F. P.: Momentum transport by gravity waves, Q. J. R. Meteorol. Soc., 95, 213–243, 1969. 5888

Broutman, D.: On internal wave caustics, J. Phys. Oceanogr., 16, 1625–1635, 1986. 5892

Cariolle, D., Muller S., Cayla F., and McCoirmick M. P.: Mountain waves, polar stratospheric clouds, and the ozone depletion over Antarctica, J. Geophys. Res., 94, D9, 11 233–11 240, 1989. 5877

Carslaw, K. S., Wirth, M., Tsias, A., Luo, B. P., Dörnbrack, A., Leutbecher, M., Volkert, H., Renger, W., Bacmeister, J. T., Reimer, E., and Peter, T.: Increased stratospheric ozone depletion due to mountain-induced atmospheric waves, Nature, 391, 675–678, 1998. 5877, 5884

Chan, K. R., Pfister, L., Bui, T. P., Bowen, S. W., Dean-Day, J., Gary, B. L., Fayey, D. W., Kelly, K. K., Webster, C. R., and May., R. D.: A case study of the mountain lee wave event of 6 January 1992, Geoph. Res. Lett., 20, 2551–2554, 1993. 5879, 5887

Dörnbrack, A., Birner, T., Fix, A., Flentje, H., Meister, A., Schmid, H., Browell, E. V., and, Mahoney, M. J.: Evidence for inertia-gravity waves forming polar stratospheric clouds over Scandinavia, J. Geophys. Res., 107, D20, 8287, doi:10.1029/2001JD000452, 2002. 5880

Dörnbrack, A., Leutbecher, M., Kivi, R., and Kyrö, E.: Mountain wave-induced record low stratospheric temperatures above northern Scandinavia, Tellus, 51A, 951–963, 1999. 5877

European Center for Medium-Range Weather Forecasts: Newsletter, 83, Reading, UK, 1999. 5879

Frei, C., Christensen, J. H., Déqué, M., Jacob, D., Jones, R. G., and Vidale, P. L.: Daily precipitation statistics in regional climate models: Evaluation and intercomparison for the European Alps, J. Geophys. Res., 108, D3, 4124, doi:10.1029/2002JD002287, 2003. 5880

Fritts, D. C. and Nastrom, G. D.: Sources of mesoscale Variability of gravity waves. Part II: frontal, convective and jet stream excitation, J. Atmos. Sci., 49, 111–127, 1991. 5878

Fueglistaler, S., Buss, S., Luo, B. P., Wernli, H., Flentje, H., Hostetler, C. A., Poole, L. R., Carslaw, K. S., and Peter, Th.: Detailed modeling of mountain wave PSCs, Atmos. Chem. Phys., 2, 697–712, 2003. 5880, 5884

Gidel, L. T. and Shapiro M. A.: The role of clear air turbulence in the production of potential vorticity in the vicinity of upper tropospheric jet stream- frontal systems, J. Atmos. Phys., 36, 2125–2138, 1979. 5894

Gossard, E. E. and Hooke W. H.: Waves in the atmosphere, Developments in atmospheric Science, Elsevier Scientific Publishing Co., Amsterdam, 456, 1975. 5878

Hanson, D. and Mauersberger, K.: Laboratory studies of nitric acid trihydrate: implications for the south polar stratosphere, Geophys. Res. Let., 15, 855–858, 1998. 5884

Hertzog, A., Souprayen, C., and Hauchecorne, A.: Observation and backward trajectory of an inertio-gravity wave in the lower stratosphere, Ann. Geophysicae, 19, 1141–1155, 2001. 5878, 5889, 5890, 5894

Herzog, H. J.: Testing a radiative upper boundary condition in a nonlinear model with hybrid vertical coordinate, Meteorol. Atmos. Phys., 55, 185–204, 1995. 5881

Hitchman, M. H., Buker, M. L., Tripoli G. J., Browell E. V., Grant W. B., Hostetler, C., McGee, T. J., and Burris, J. F.: Nonorographic generation of Arctic polar stratospheric clouds during December 1999, J. Geophys. Res., 108, D5, 8325, doi:10.1029/2001JD001034, 2003. 5877, 5878, 5897

Kaplan, M. L. and Paine, D. A.: The observed divergence of the horizontal velocity field and pressure gradient force at the mesoscale: its implications for the parameterization of three-

dimensional momentum transport in synoptic scale numerical models, Beitr. Phys. Atmos., 50, 321–330, 1977. 5885
Klemp, J. B. and Durran D. R.: An upper boundary condition permitting internal gravity wave radiation in numerical mesoscale models, Mon. Wea. Rev., 111, 430–444, 1983. 5881
Knox, J. A.: Possible mechanisms of clear-air turbulence in strongly anticyclonic flows, Mon. Wea. Rev., 125, 1251–1259, 1996. 5878, 5885, 5896
Koop, T., Luo B. P., Tsias A., and Peter T.: Water activity as the determinant for homogeneous ice nucleation in aqueous solutions, Nature, 406, 611–614, 2000. 5883
Leutbecher, M. and Volkert, H.: The propagation of mountain waves into the stratosphere: quantitative evaluation of three dimensional simulations, J. Atmos. Sci., 57, 3090–3108, 2000. 5879
Luo B. P., Voigt, C., Fueglistaler, S., and Peter, Th.: Extreme NAT supersaturations in mountain wave ice PSCs – a clue to NAT formation, J. Geophys. Res., 108, D15, 4441, doi:10.1029/2002JD003104, 2003. 5877, 5884, 5886
Lüthi, D., Cress, A., Davies H. C., Frei C., and Schär, C.: Interannual variability and regional climate simulations, Theor. Appl. Climatol., 53, 185–209, 1996. 5880
Lüthi, S.: Idealisierte Gebirgsüberströmung in einem operationellen numerischen Modell, Diploma Thesis, ETH Zürich, 141, 1994. 5881
Majewski, D.: The Europa-Model of the DWD, ECMWF seminar on numerical methods in atmospheric science, 147–191, 1991. 5880
Nastrom, G. D., Van Zandt, T. E., and Warnock J. M.: Vertical wavenumber spectra of wind and temperature from high resolution balloon soundings over Illinois, J. Geophys. Res., 102, 6685–6701, 1997. 5878
O'Sullivan, D. and Dunkerton, J.: Generation of inertio-gravity waves in a simulated life cycle of baroclinic instability, J. Atmos. Sci., 52, 3695–3716, 1995. 5878, 5890, 5894, 5895, 5899
Pavelin, E. J., Whiteway A., and Vaughan G.: Observation of gravity wave generation and breaking in the lowermost stratosphere, J. Geophys. Res., 108, 5173–5179, 2001. 5878
Peters, D., Hoffmann, P., and Alpers, M.: On the appearance of inertio-gravity waves on the North-Easterly side of an anticyclone, Meteor. Zeitschrift, 12, 25–35, 2003. 5878
Rabier, F., Järvinen, H., Klinker, E., Nahfouof, J.-F., and Simmons, A.: The ECMWF operational implementation of four dimensional variation assimilation. Part I: Experimental results with simplified physics, Q. J. R. Meteorol. Soc., 126, 1143–1170, 2000. 5879
Scinocca, J. F. and Ford, R.: The nonlinear forcing of large-scale internal gravity waves by

stratified shear instability, J. Atmos. Sci., 57, 653–672, 2000. 5879
Schwierz C.: Interactions of Greenland-scale orography and extra-tropical synoptic-scale flow, Diss. ETH No. 4356, 2001. 5884
Scott, S. G., Chan, K. R., Bowen, S. W., and Bui, T. P.: The Meteorological Measurement System on the NASA ER-2 aircraft, J. Atmos. Oceanic Technol., 7, 525–540, 1990. 5887
Shibata, T., Sato, K., Kobayashi, H., Yabuki, M., and Shiobara, M.: Antarctic polar stratospheric clouds under temperature perturbations by nonorographic inertia gravity waves observed by micropulse lidar at Suowa station, J. Geophys. Res., 108, D3, 4105, doi:10.1029/2002JD002713, 2003. 5878, 5884, 5897
Sutherland, B. R. and Peltier W. R.: Internal gravity-wave emission into the middle atmosphere from a model tropospheric jet, J. Atmos. Sci., 52, 3214–3235, 1995. 5878
Thomas, L., Worthington R. M., and McDonald, A. J.: Inertia-gravity waves in the troposphere and lower stratosphere associated with a jet stream exit region, Ann. Geophysicae, 17, 115–121, 1999. 5878, 5894
Uccellini, L. W. and Koch, S. E.: The synoptic setting and possible energy sources for mesoscale wave disturbances, Month. Weath. Rev., 115, 721–729, 1987. 5878, 5897
Wernli, H. and Davies, H. C.: A Lagrangian-based analysis of extratropical cyclones. I: The method and some applications, Q. J. R. Meteorol. Soc., 123, 467–489, 1997. 5883
Whiteway, J. A. and Duck, T. J.: Enhanced Arctic stratospheric gravity wave activity above a tropospheric jet, Geophys. Res. Let., 26, 2453–2456, 1999. 5885
Zhang, F., Koch, S. E., Davis, C. A., and Kaplan, M. L.: A survey of unbalanced flow diagnostics and their application, Adv. Atmos. Sci., 17, 165–183, 2000. 5894

Table 1. Gravity wave packet specifications and uncertainties.

Θ	ω_0/f	λ_x [km]	λ_y [km]	λ_z [km]
-173±4°	3.3 ± 1.0	387	3149	8±1.2

ACPD

3, 5875–5918, 2003

Table 2. Summary of the numerical experiments conducted with the mesoscale model HRM. T_{min}^{ICE} stays for the temperature at the time and location of maximum observed BSR and on the 25.3 hPa level, T_{min}^{DC8} is the minimum temperature at the same location at any height. and T_{min}^{ER2} is the minimum temperature where the ER-2 observed a local minimum in the temperature.

Simulation	T_{min}^{ICE}	T_{min}^{DC8}	$p(T_{min}^{DC8})$	T_{min}^{ER2}
Initial. 12 January 12:00 UTC	−88.6	−88.9	23.8	−81.8
Initial. 12 January 18:00 UTC	−87.3	−87.4	26.4	−82.6
Initial. 13 January 00:00 UTC	−88.5	−88.9	23.8	−83.6
Initial. 13 January 06:00 UTC	−89.6	−89.7	23.8	−84.0
control run	−91.2	−91.3	23.8	−82.6
Initial. 13 January 18:00 UTC	−88.2	−88.3	21.4	−83.1
Initial. 14 January 00:00 UTC	−83.9	−84.9	19.3	−82.0
30 vertical levels	−85.7	−87.3	15.6	−83.8
double mesh-widths	−93.0	−93.7	21.4	−83.6
10x diffusion	−87.7	−87.8	21.4	−84.0
moist physics	−89.8	−89.8	21.4	−84.0
conv no rad	−90.9	−91.0	23.8	−84.1

ACPD
3, 5875–5918, 2003

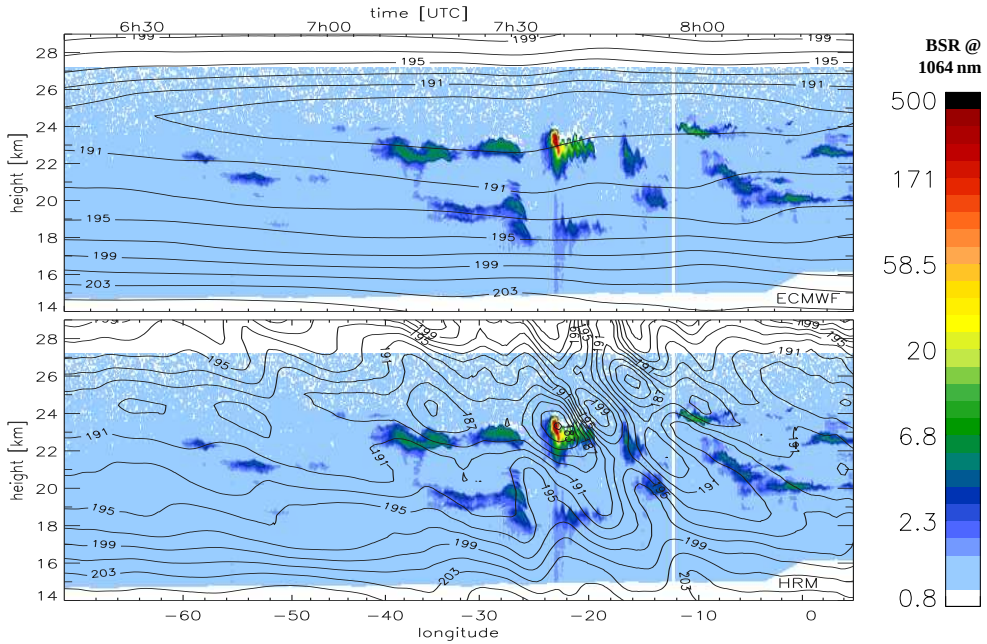

Fig. 1. Backscatter ratio (BSR) at 1064 nm from the DC-8 LaRC lidar during a flight over GL on 14 January 2000. Overlayed are the 4-D interpolated temperature fields from (top) the ECMWF analyses and (bottom) the HRM mesoscale model simulation. The flight path is shown by the orange line in Fig. 4 (top).

ACPD
3, 5875–5918, 2003

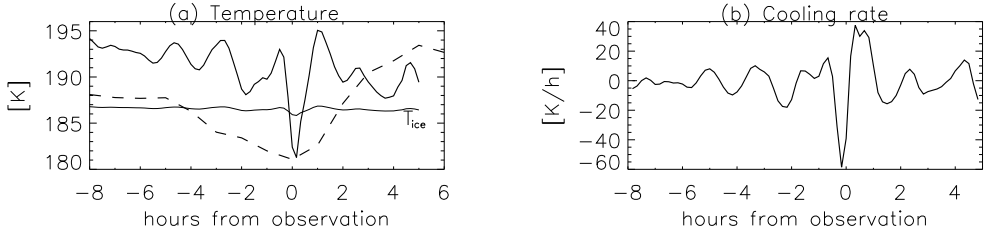

Fig. 2. Temperature **(a)** and cooling rate in Kh^{-1} **(b)** along the air trajectory started at the time and location of maximum observed BSR. The dashed line in panel (a) indicates the time evolution of HRM temperature at the trajectory's starting point.

ACPD
3, 5875–5918, 2003

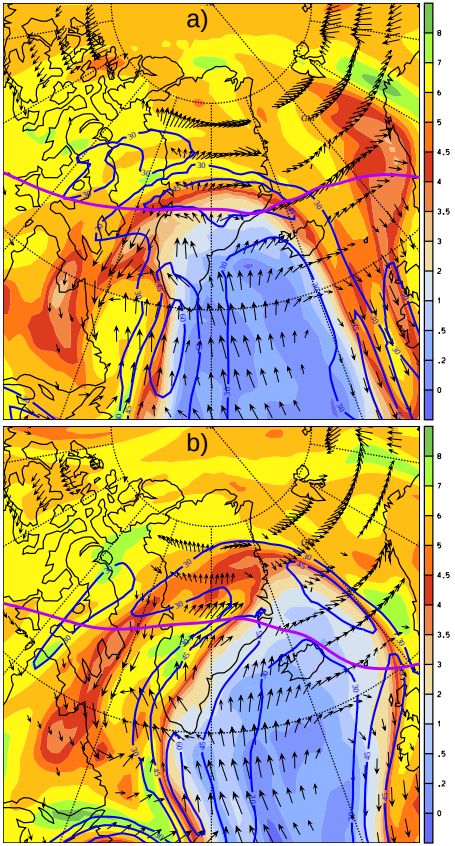

Fig. 3. The synoptic situation on 13 January, 18:00 UTC **(a)** and 14 January, 06:00 UTC **(b)** from ECMWF analysis data. Color: potential vorticity [pvu] at 320 K, blue contours: wind speed at 370 hPa (isolines for 30, 45 and 60 m s^{-1}) and black vectors: wind vectors at the model lowermost level if velocity >5 m s^{-1}, south of 80° N. The violet contour denote the vortex edge on the 665 K isentrope.

ACPD
3, 5875–5918, 2003

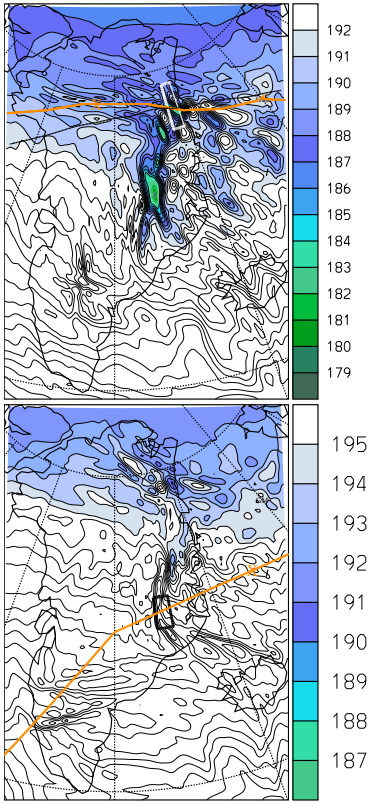

Fig. 4. Mesoscale temperature [K] fields (green stands for $T < T_{ice}$, and blue for $T < T_{nat}$) from the HRM simulation on 14 January 2000, 07:00 UTC (23 km height, top) and 18:00 UTC, at the cruise altitude of the ER2 (19.3 km, bottom). Orange overlayed lines are the DC-8 (top) and ER-2 flight pathes (bottom). The crosses denote the locations of the airplanes at the model output time. The emphasized boxes show the domains for the wind average calculations shown in Fig. 6. The black line in the top panel is the horizontal trace of the air trajectory shown in Fig. 2.

ACPD
3, 5875–5918, 2003

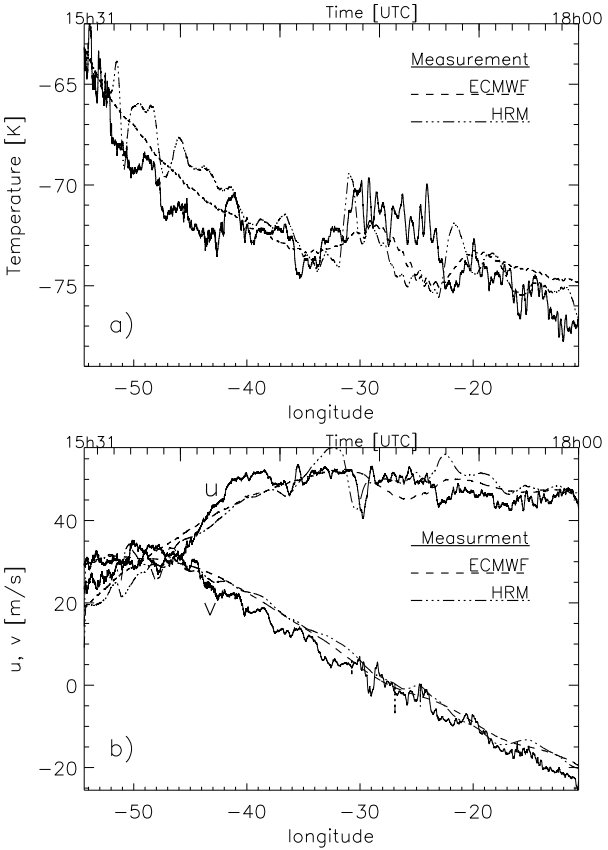

Fig. 5. Temperature **(a)** and zonal and meridional wind **(b)** measurement aboard the ER-2 aircraft on 14 January 2000 (1 s resolution) within the mesoscale simulation domain as well as ECMWF and HRM temperatures along the flight path which is shown in Fig. 4 (bottom).

ACPD
3, 5875–5918, 2003

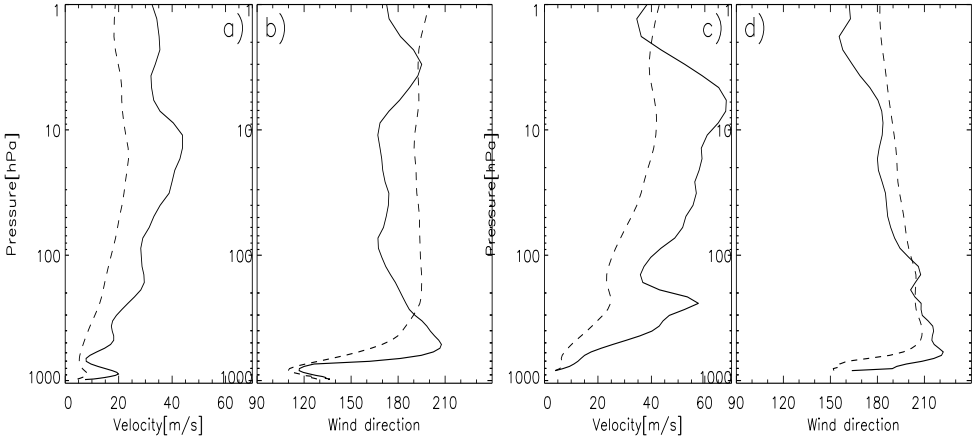

Fig. 6. Domain averaged ECMWF wind velocity **(a), (c)** and direction **(b), (d)**; westerlies corresponding to 180°). Panels (a) and (b) are for "wave DC8" at 00:00 UTC 14 January (see box in Fig. 4, top), and panels (c) and (d) for "wave ER2" at 12:00 UTC 14 January (see box in Fig. 4, bottom). Dashed lines show the January 2000 mean wind profiles in the same boxes.

ACPD
3, 5875–5918, 2003

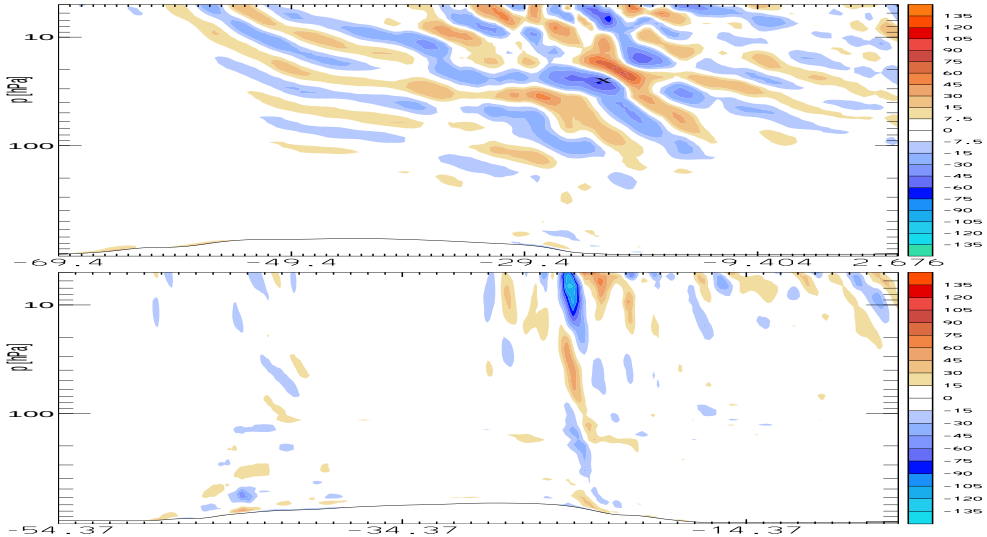

Fig. 7. HRM-Divergence (blue) and convergence ($10^{-5}\,s^{-1}$) field along the DC-8 (top, 07:00 UTC) and ER-2 (bottom, 18:00 UTC) flight paths on 14 January 2000 as a function of longitude and pressure. The black cross in the upper panel shows the location of the observed ice PSC.

ACPD
3, 5875–5918, 2003

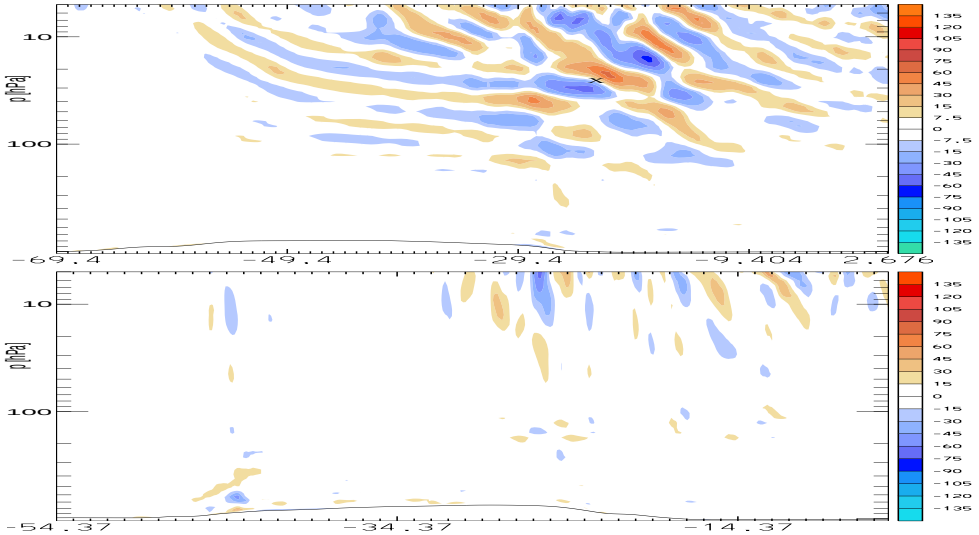

Fig. 8. Same as Fig. 7 but for a HRM simulation for which the orography has been uniformly reduced by 25%.

ACPD
3, 5875–5918, 2003

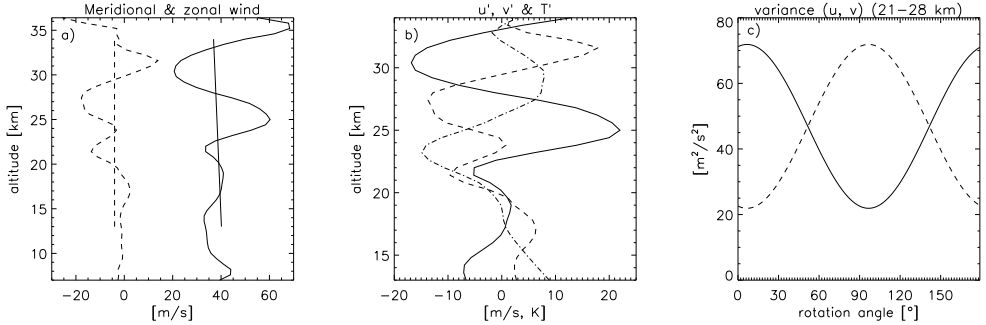

Fig. 9. Vertical profiles (using HRM data) at the location (22.6 W, 77.3 N) and time (08:00 UTC) of maximum BSR observation. Panel **(a)** shows the zonal (solid) and meridional (dashed) wind components along with their (13–34 km height) fitted first order polynomial (thin lines), while the deviations thereto are represented in panel **(b)** along with the analogue temperature fluctuations (dash-dotted line). The parallel (solid) and perpendicular (dashed) wind variances are revealed as a function of the propagation angle in panel **(c)**.

ACPD
3, 5875–5918, 2003

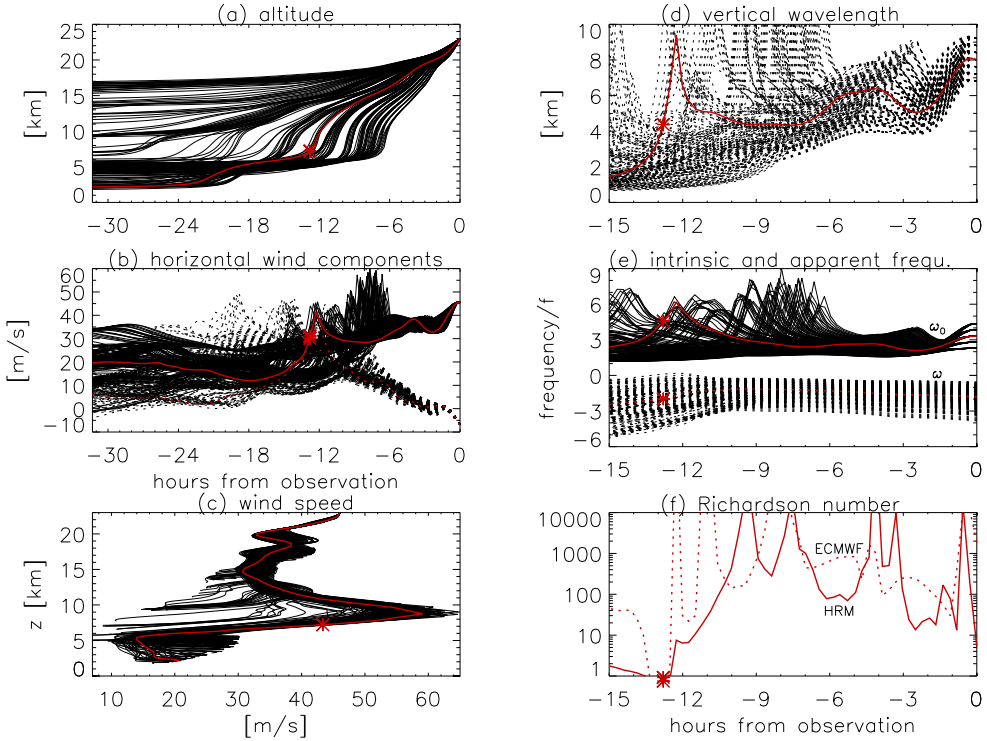

Fig. 10. Variables along the 175 backward ensemble ray trajectories: **(a)** altitude, **(b)** meridional (dashed) and zonal wind components from ECMWF analyses, **(c)** zonal and meridional (dashed) wavelengths, **(d)** vertical wavelength, **(e)** Richardson number from ECMWF (dashed) and HRM and **(f)** intrinsic and apparent (dashed) frequencies. The most likely trajectory is displayed in red. The stars show the supposed time of generation (see text).

ACPD
3, 5875–5918, 2003

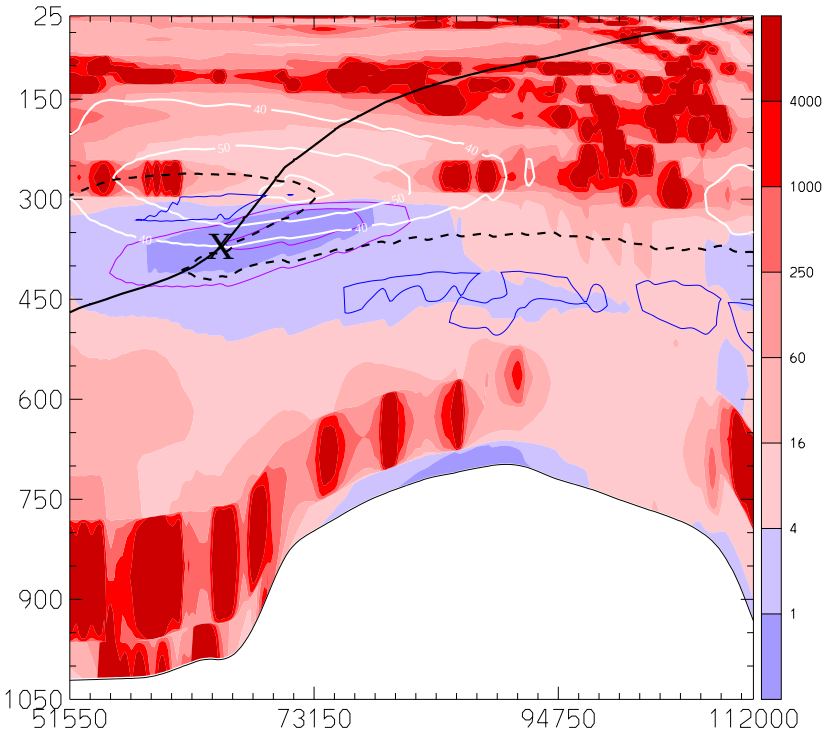

Fig. 11. Four-dimensional linear interpolation of the Richardson number (colors) from the HRM data along the ray-trajectory which is indicated by the black line as a function of pressure and time (seconds from 13 January, 00:00 UTC). The cross denotes the minimum Richardson number along the trajectory and the possible location of wave generation (see text). The white contours denote the wind velocity (contours for 40, 50 and 60 ms^{-1}); the violet contour show the positive vertical shear (contours for 12.5 and 17.5 $\cdot 10^{-3} s^{-1}$); the blue contour tropospheric low static stability regions ($N^2 = 1.25 \cdot 10^{-4} s^{-2}$) and the dotted black curve shows the tropopause (defined by the PV=2 pvu potential vorticity isosurface).

ACPD
3, 5875–5918, 2003

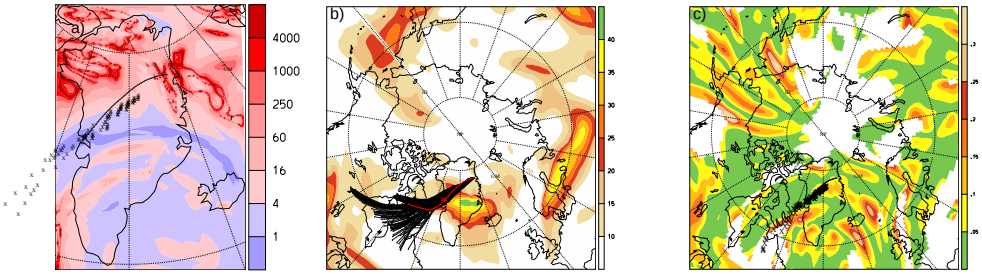

Fig. 12. Three jet instability diagnostics: the Richardson Number **(a)** computed with HRM data at the presumed time of "wave DC8" generation, 13 January, 19:00 UTC, the residual from Eq. (4) (10^{-5} s^{-2}) **(b)** both on the 370 hPa surface and the Lagrangian Rossby number **(c)** on the 300 K isentropic surface. The two latter diagnostics computed with ECMWF data for 13 January, 18:00 UTC. In panel (b) the ensemble rays are shown in full length, in red for the "first guess ray" and in the other panels, the horizontal trace of the "first guess ray" is indicated by the black line until its supposed generation and the crosses mark the location where the ensemble ray trajectories cross the depicted horizontal surfaces.

ACPD
3, 5875–5918, 2003

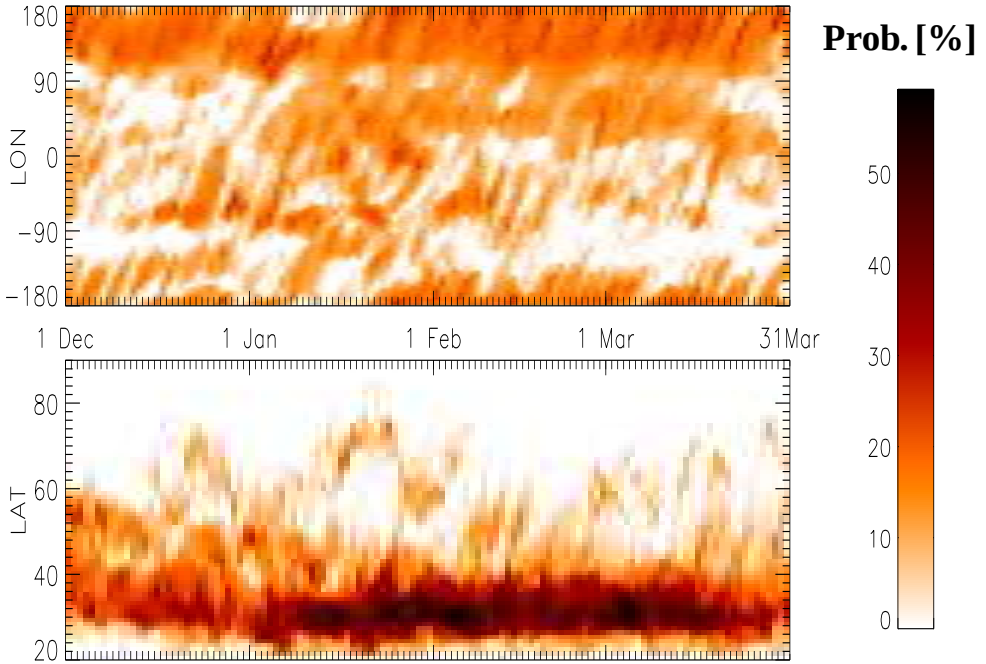

Fig. 13. Winter 1999/2000 climatology of potential jet instabilities computed with the residual of the non-linear balance equation (Eq. 4) and ECMWF analyses fields. The probability depicted in the upper (lower) panel is that at least on one model level in the 500–100 hPa range, the residual of the NBE exceeds 40 s^{-2} for all latitudes (longitudes) and every ECMWF output within a given day.

ACPD
3, 5875–5918, 2003